
Supplementary information

**Genetically encoded photo-switchable
molecular sensors for optoacoustic and
super-resolution imaging**

In the format provided by the
authors and unedited

Supporting Information

Prototyping genetically encoded photo-switchable indicators, new tools for optoacoustic imaging and fluorescence nanoscopy.

Kanuj Mishra^{a+}, Juan Pablo Fuenzalida-Werner^{ab+}, Francesca Pennacchietti^{c§}, Robert Janowski^{d§}, Andriy Chmyrov^{ae}, Yuanhui Huang^{ae}, Christian Zakian^{ae}, Uwe Klemm^a, Ilaria Testa^c, Dierk Niessing^{df}, Vasilis Ntziachristos^{aeg}, Andre C. Stiel^{a*}

- a) Institute of Biological and Medical Imaging (IBMI), Helmholtz Zentrum München, D-85764 Neuherberg, Germany
- b) Chair of Biogenic functional materials, Technische Universität München, 94315 Straubing, Germany
- c) Science for Life Laboratory, KTH Royal Institute of Technology, 17165 Stockholm, Sweden
- d) Intracellular Transport and RNA Biology Group, Institute of Structural Biology, Helmholtz Zentrum München, D-85764 Neuherberg, Germany
- e) Chair of Biological Imaging at the Center for Translational Cancer Research (TranslaTUM), School of Medicine, Technical University of Munich, D-81675 München, Germany
- f) Institute of Pharmaceutical Biotechnology, D-89081 Ulm University, Ulm, Germany
- g) Munich Institute of Robotics and Machine Intelligence (MIRMI), Technical University of Munich, Germany, D-81675 München, Germany

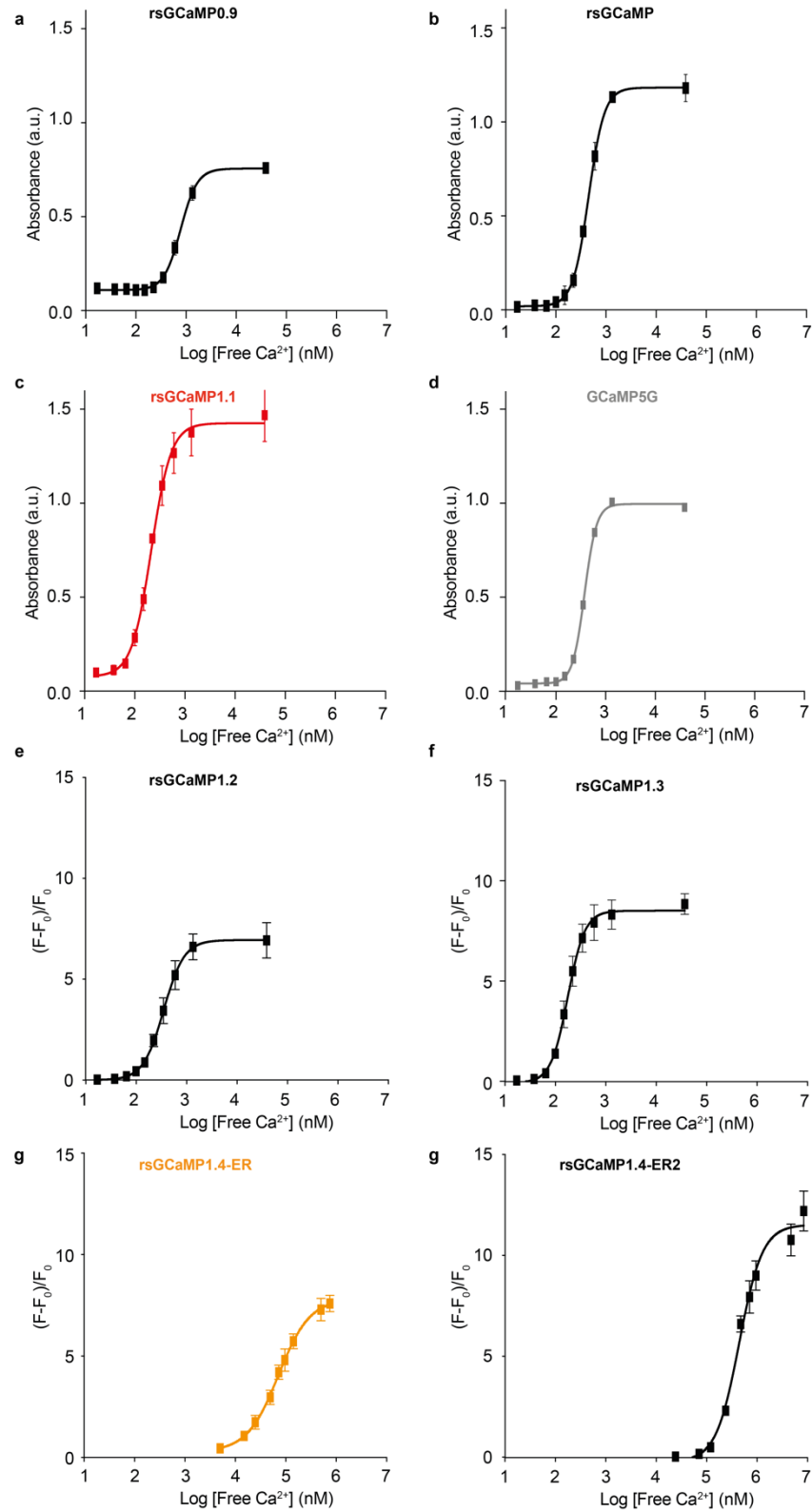
+/§)K.M. and J.P.F-W. as well as F.P. and R.J. contributed equally to this work

*) Correspondence should be addressed to A.C.S. (andre.stiel@helmholtz-muenchen.de)

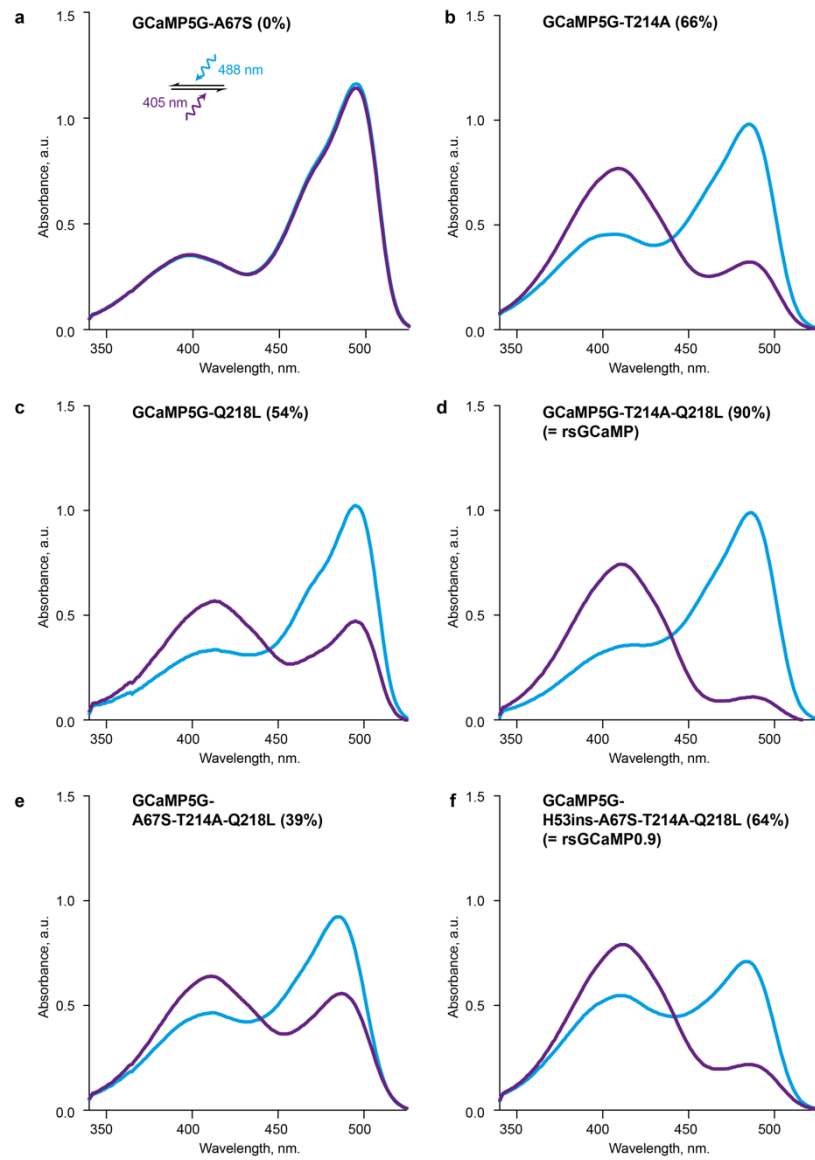
Supporting Information 1: Details on the engineering process of rsGCaMPs.

Our rsGCaMPs were engineered based on the conventional calcium indicator GCaMP5G and mutational insights from the development of GFP-based reversible switchable proteins rsEGFP and rsEGFP2. As a first step, structural observations based on rsEGFP2 led to the rational design of a GCaMP5G variant with mutations A67S, T214A and Q218L (Extended Data Table 1a and 1b, and Supplementary Figures 1-3). This variant already exhibited reversible switching upon illumination, with a signal change of ~39% at 488 nm, while preserving the calcium sensitivity of GCaMP5. Attempts to improve the switching by mutating positions in the vicinity of key residues (G79A, V54A, T129I and A67R) on the basis of variant GCaMP5G-A67S+T214A+Q218L did not lead to any significant change.

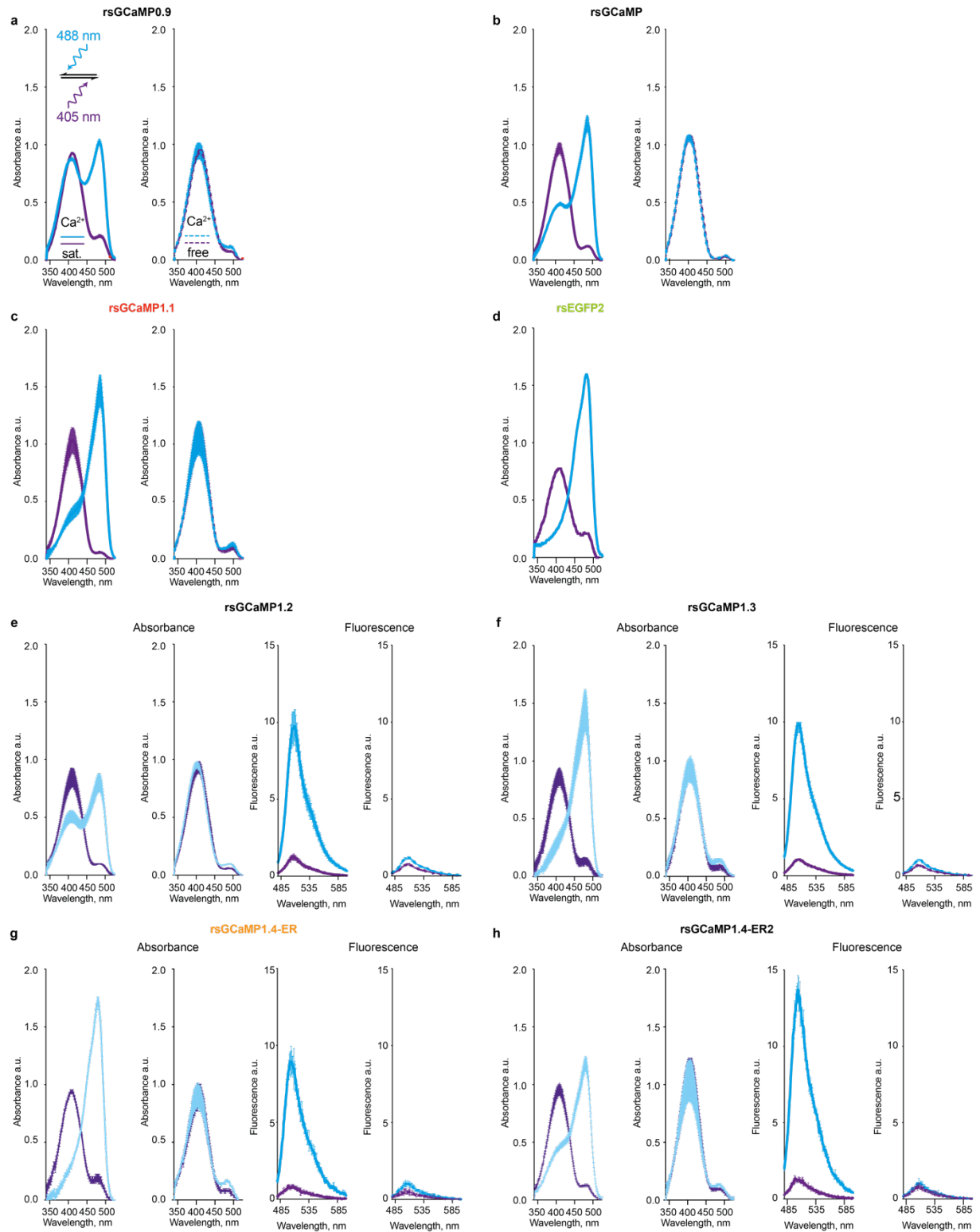
Based on the rationale that H148 of GFP is missing in GCaMPs (due to the cpGFP), we introduced this residue into the triple variant to produce rsGCaMP0.9 (GCaMP5G-H53ins+A67S+T214A+Q226). Variant rsGCaMP0.9 showed a promising ~65% signal change at 488 nm between the ON and OFF states in the Ca^{2+} saturated state and an 83% signal change between the Ca^{2+} bound and unbound states. Subsequently, we removed individual mutations to probe their effects. We found that the A67S mutation was detrimental because it completely prevents switching in double mutants with T214A or Q218L. In contrast, the single variants T214A and Q218L show 66% and 54% photo-switching in the Ca^{2+} saturated form, respectively. Lastly, we compared the triple mutant H53ins+T214A+Q226 with the double mutant T214A+Q226. Surprisingly, the double mutant shows similar calcium sensitivity to GCaMP5G and superior switching compared to our earlier variants, with a ~90% signal change between the ON and OFF states in the Ca^{2+} saturated form. Consequently, we used the double mutant for our variant rsGCaMP. Based on modifications made while attempting crystallization, we realized that the mutations L294T and P295R in the linker region towards the Calmodulin part further improved the switching dynamic range (rsGCaMP1.1). Due to the relatively low fluorescence quantum yield (QY) and high absorptivity, we used this variant for the optoacoustic proof-of-concept experiments. To facilitate fluorescence super-resolution microscopy experiments we introduced a number of mutations stabilizing the ON state chromophore (I71, V107 positions in GCaMP5G and I168 and T204 in rsEGFP2, respectively), eventually yielding rsGCaMP1.3 and rsGCaMP1.4. For the latter, we constructed further variants with Ca^{2+} affinities suitable for measurements in the endoplasmic reticulum (rsGCaMP1.4ER and rsGCaMP1.4ER2), with affinities of 72 and 465 μM , respectively. The introduced mutations were based on GCaMP6-150¹ and GCaMP_{er}².



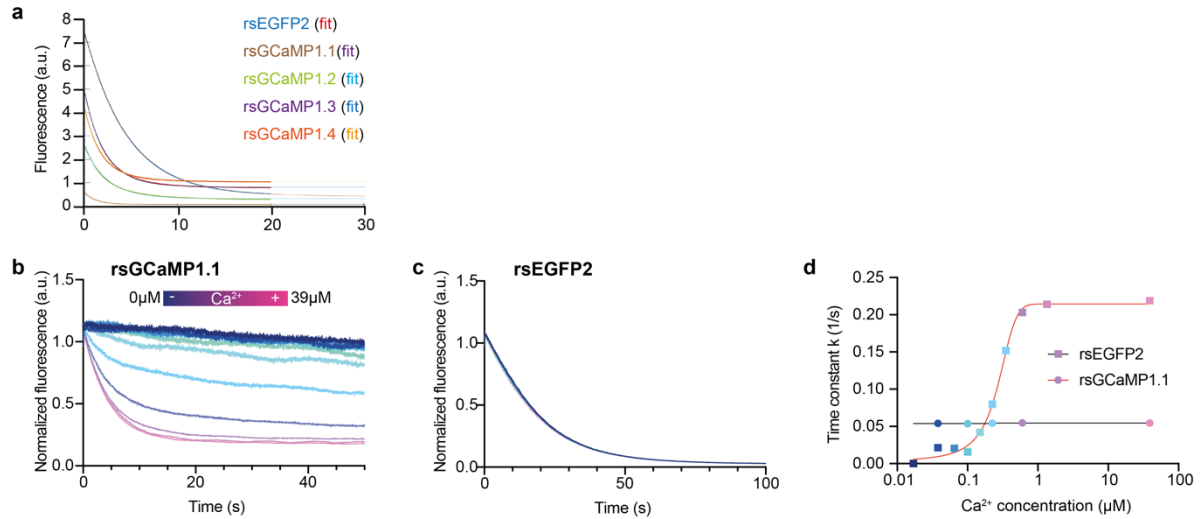
Supplemental Figure 1: Ca^{2+} concentration dependent response in absorbance (a-d) or fluorescence (e-h) for variants developed and proteins discussed in this work. All Ca^{2+} dependencies were measured after fully switching the protein to the ON state with light as described in Extended Data Table 1. The mean values and standard deviation are shown for three independent replicates (n=3).



Supplemental Figure 2: Photo-switching of initial variants at Ca^{2+} saturation. Absorbance spectra are shown after prolonged illumination with 488 nm light in the OFF-state (purple lines) or 405 nm light in the ON-state (blue lines). Dynamic range at 488 nm is given in brackets. The concentration of Ca^{2+} in the saturated solution is 39 μM . Spectra are derived from single experiments ($n=1$). For the variants that are further discussed in the presented work, measurements of triplicates are shown in Supplemental Figure 3. Photo-switching details are given in Extended Data Table 1.



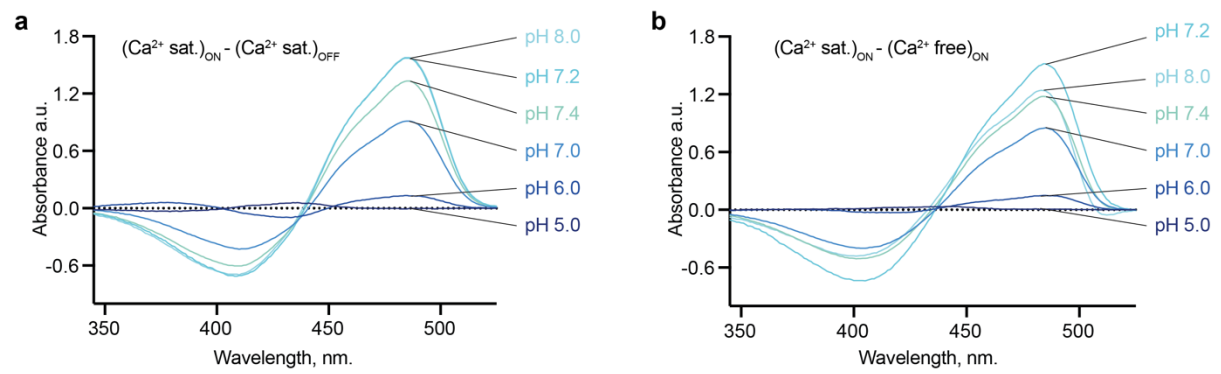
Supplemental Figure 3: Photoswitching of major variants developed and discussed in this work recorded as absorbance (a-d) or absorbance and fluorescence spectra (e-h). Spectra are given as the mean and standard deviation for three independent replicates ($n=3$). Absorbance spectra are normalized for the protein absorbance maxima at ~ 280 nm while fluorescence spectra are normalized by the signal without Ca^{2+} . For each variant, the spectra are shown in the Ca^{2+} -saturated ($39 \mu\text{M Ca}^{2+}$, solid lines, left panels) and Ca^{2+} -free forms (dashed lines, right panels), and after prolonged illumination with 488 nm light in the OFF-state (purple lines) or 405 nm light in the ON-state (blue lines). The fluorescence spectra are shown only for variants exhibiting significant fluorescence (two rightmost panels of each item in e-h). Photo-switching details are given in Extended Data Table 1.



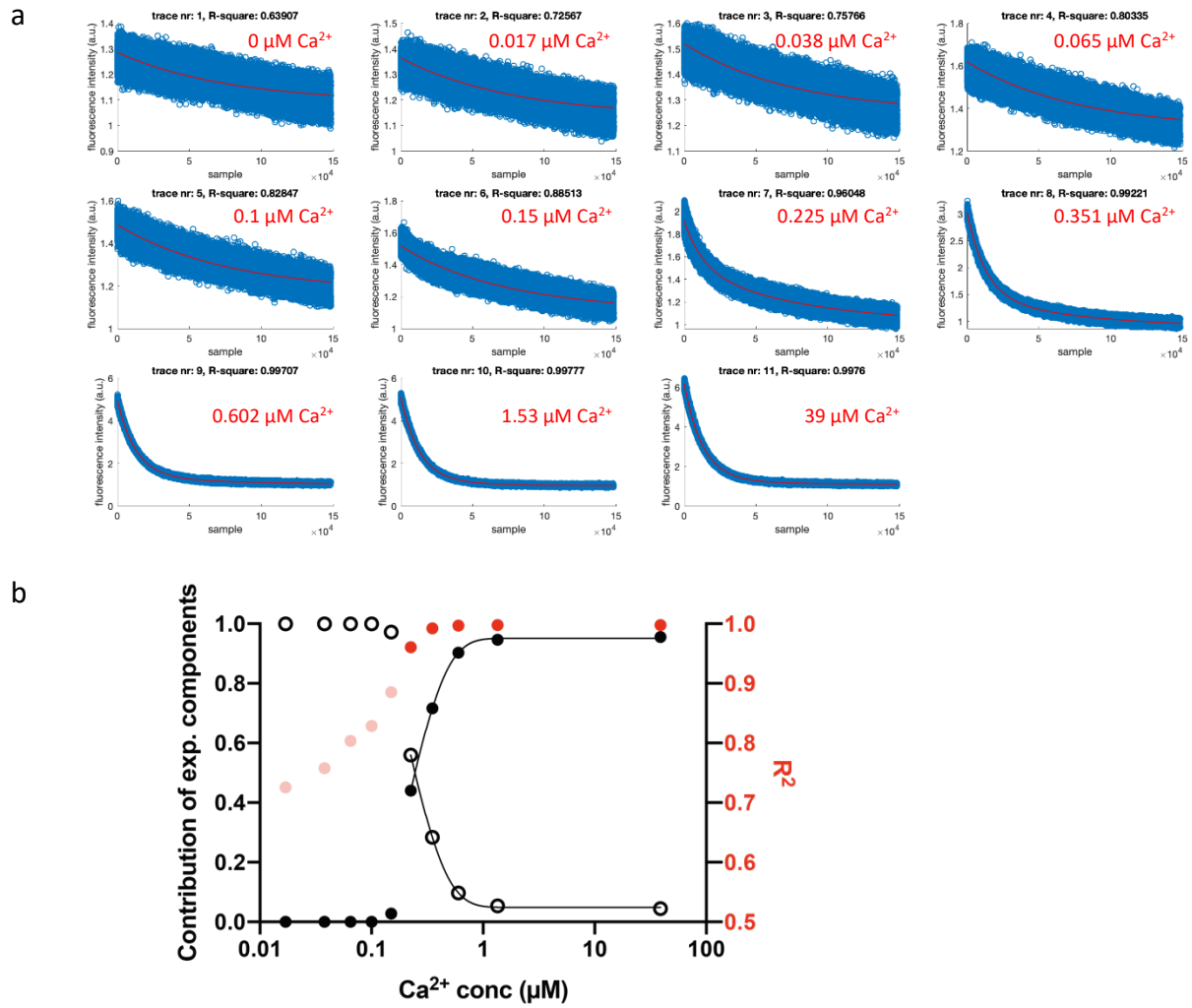
Supplemental Figure 4: Fluorescence switching kinetics of rsEGFP2 and rsGCaMP variants.

a Photoswitching kinetics of selected variants. The mean values of 10 switching-cycles are shown with a single exponential fit for the data. The data is from single experiment ($n=1$). Protein and Ca^{2+} concentrations are 15 μM and 39 μM (saturated), respectively. **b** Representative photoswitching traces ($n=1$) of 25 μM purified rsGCaMP1.1 under different Ca^{2+} concentrations (0 μM ; 0.017 μM ; 0.038 μM ; 0.065 μM ; 0.1 μM ; 0.15 μM ; 0.225 μM ; 0.351 μM ; 0.602 μM ; 1.53 μM ; 39 μM). **c** Representative photoswitching traces ($n=1$) photoswitching traces of 45 μM rsEGFP2 at selected Ca^{2+} concentrations (0 μM ; 0.038 μM ; 0.1 μM ; 0.225 μM ; 0.351 μM ; 0.602 μM ; 39 μM). **d** Sigmoidal fits of the time constants from (b) and (c). Photoswitching was carried out on pure protein in the Ca^{2+} saturated state using 405/12 nm or 470/34 nm LEDs (Thorlabs), 488/10 nm and 405/10 nm bandpass filters, and a 10x objective lens in defocus covering a 5 mm diameter well. Energies at the sample were 13 mW/cm^2 and 14 mW/cm^2 at 405 nm and 488 nm, respectively.

Although the mechanism of rsGCaMPs calls for fits with multiple (most likely two) exponentials (Supporting Information 2), we fit the data here only with a single exponential because it was very noisy, particularly at low Ca^{2+} concentrations, and we sought to treat all data uniformly.



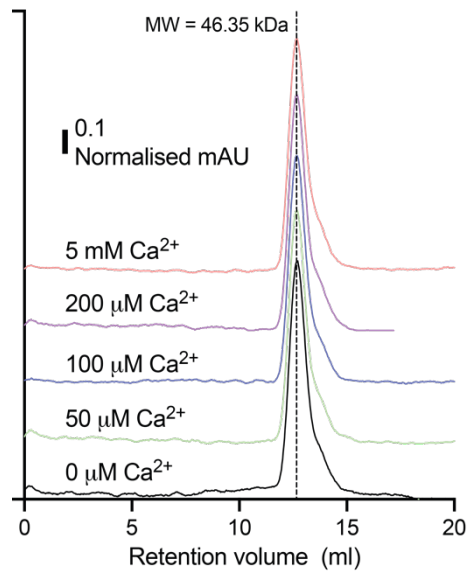
Supplemental Figure 5: pH dependence of variant rsGCaMP1.1 in regard to photo-switching (a) and Ca^{2+} response (b). Ca^{2+} is saturated is $39 \mu\text{M}$. Photo-switching details are given in Extended Data Table 1. Data is from $n=1$ measurement.



Supplemental Figure 6: Fitting of data with multiple exponential. a Bi-exponential fits of switching traces of rsGCaMP1.1, measured in a fluorescent microscope on pure protein (15 μM) with different Ca^{2+} concentrations (1 to 11: 0 μM ; 0.017 μM ; 0.038 μM ; 0.065 μM ; 0.1 μM ; 0.15 μM ; 0.225 μM ; 0.351 μM ; 0.602 μM ; 1.53 μM ; 39 μM). Shown is the mean of 10 switching cycles of a single experiment ($n=1$). All fits were performed with the same time constants. The time constants have been optimized by a least squares fit procedure minimizing the R^2 for traces 8 to 11 (0.351 μM ; 0.602 μM ; 1.53 μM ; 39 μM). **(b)** Sigmoidal fits for the contribution of the fast (full circles) and slow time constants (empty circles) obtained for the data shown in **a**, together with the R^2 for the respective exponential fits. For the sigmoidal fits, only data points with $R^2 > 0.9$ were used (full red circles). The drop in R^2 suggests that either a bi-exponential model does not fully explain the switching kinetics or that the low Ca^{2+} concentration data is too noisy. Fits with multi-exponential models and a shared time-constant over the whole dataset did not converge.

Supporting Information 2: Multi species rationale.

Fluorescence switching curves at different Ca^{2+} concentrations can be globally fitted for higher concentrations with a bi-exponential model (Supplemental Figure 6), with fixed time constants and variable amplitudes; this behavior suggests that at least two distinct species are involved in tailoring the Ca^{2+} response. We further confirm this by fluorescence lifetime measurements (Extended Data Figure 1) that show two main components with their amplitudes determined by the Ca^{2+} concentration. The excited-state lifetime of a molecule does not vary with the molecule's concentration. Therefore, if only one emitting species is present then no change in excited state lifetime is expected. Changes in lifetime due to Ca^{2+} concentrations can only be understood as chromophores having different conformations and/or interactions with the nearby amino acids that are determined by the Ca^{2+} concentration. For rsGCaMPs at least two species are involved (as suggested in model Extended Data Figure 2d).



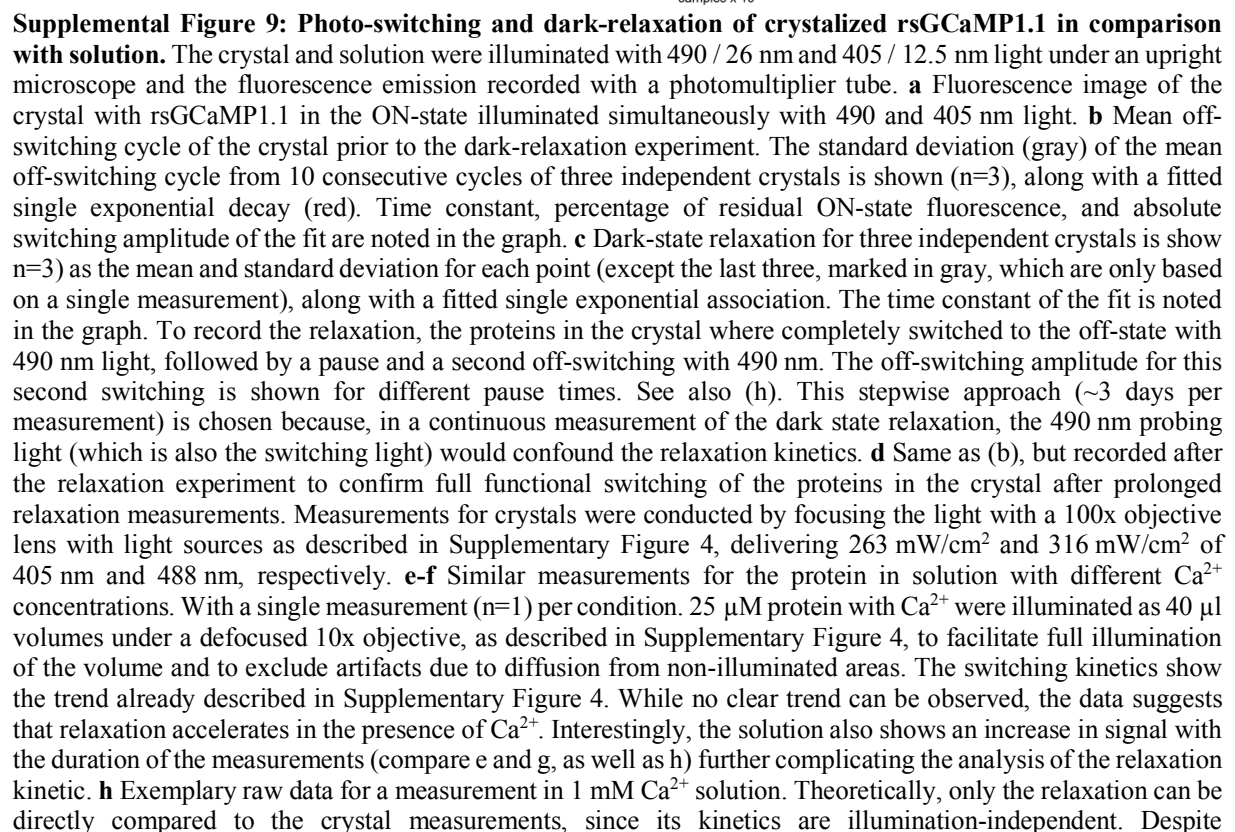
Supplemental Figure 7. Analytical Size exclusion chromatography for rsGCaMP1.4ER. Protein was measured at high concentration (15 mg/ml) and low salt conditions (50 mM NaCl) to confirm low aggregation tendencies. Protein solutions were measured at Ca^{2+} concentrations ranging from 0 to 5 mM as indicated in the graph. Data is from a single chromatography run per condition (n=1).



Supplemental Figure 8: Swapped Dimer Structures. Several crystallization attempts yielded swapped dimer structures also described by e.g. Akerboom, 2009⁹ and Chen, 2013¹⁰. As an example, we show here the structure of rsGCaMP0.9. Dimers colored differently; both chromophores in yellow.

Supplemental Table 1: Variants of rsGCaMP generated and crystallized.

Code	Protein variant	Crystallization condition		Unit cell parameters a, b, c, α , β , γ	Space group	Monomers per asym. unit
P751	rsGCaMP	0.2 Ammonium acetate, 0.1 M Bis-Tris pH 5.5, 25% w/v PEG 3350	Dimer	126.25, 46.19, 68.35, 90.00, 100.71, 90.00	C2	1
P758	rsGCaMP G87R	0.15 Magnesium formate, 17% w/v PEG 3,350	Dimer	66.76, 60.10, 117.92, 90.00, 92.70, 90.00	P2 ₁	2
P759	rsGCaMP RSET Truncated	0.2 M Lithium sulphate, 0.1 M Bis-Tris pH 6.5 25% w/v PEG 3,350	Dimer	126.54, 47.00, 68.80, 90.00, 100.83, 90.00	C2	1
P660_SET4	rsGCaMP0.9 RSET Truncated	0.15 M Magnesium formate and 17% w/v PEG 3,350	Dimer	128.12, 47.61, 68.44, 90.00, 102.48, 90.00	C2	1
P660	rsGCaMP0.9	0.15 M Magnesium formate, 17% w/v PEG 3,350	Dimer	129.01, 47.67, 68.729, 90.00, 102.51, 90.00	C2	1
P660	rsGCaMP0.9	0.15 M Magnesium formate, 17% w/v PEG 3,350	Dimer	127.87, 47.56, 68.96, 90.00, 101.83, 90.00	C2	1
P660	rsGCaMP0.9	0.10% w/v n-Octyl-b-D-glucoside, 0.1 M Sodium citrate tribasic dihydrate pH 5.5, 22% w/v PEG 3,350	Dimer	128.05, 47.15, 87.06, 90.00, 115.70, 90.00	C2	1
P705	rsGCaMP0.9 G79R	0.05 M Sodium cacodylate pH 6.5, 0.01 M Magnesium sulfate, 2 M Ammonium sulfate	Dimer	93.29, 255.79, 157.72, 90.00, 90.00, 90.00	C 2 2 2 ₁	4
P708	rsGCaMP0.9 V108L	0.16 M Calcium Acetate, 0.06M Sodium cacodylate pH 6.5, 14% w/v PEG 8,000, 20% v/v glycerol	Dimer	128.11, 47.08, 86.65, 90.00, 115.32, 90.00	C2	1
P776	rsGCaMP RSET truncated, L295T, P296R (rsGCaMP-Xtal)	0.21 M Sodium formate, 0.1 M Bis-Tris-Propane pH 8.5, 18% (w/v) PEG 3350	Monomer	119.43, 119.43, 96.62, 90.00, 90.00, 90.00	P 4 ₁ 2 ₁ 2	



confounders in the solution measurements, the crystal and solution show a difference in relaxation kinetics of 10x to 5x, depending on the concentration of Ca^{2+} . We assume that this difference is due to the crystal having a constant, fully enclosed chromophore, since the sensor is “permanently bound to Ca^{2+} ” due to the crystallization – “simplifying the possible effects” (See also explanation in Extended Data Figure 2). In contrast, for the solution, Ca^{2+} concentration seems to affect the relaxation kinetics similar as the photoswitching kinetics due to binding/unbinding events.

Despite the mechanism of rsGCaMPs calling for fits with multiple (most likely two) exponentials (as shown and explained in Suppl. Figure 6, Extended Data Figure 1-2 and Supporting Information 2) we fit here only with a single exponential, since especially the data at low Ca^{2+} concentrations are very noisy. We fit everything here with a single exponential so as to treat all data uniformly.

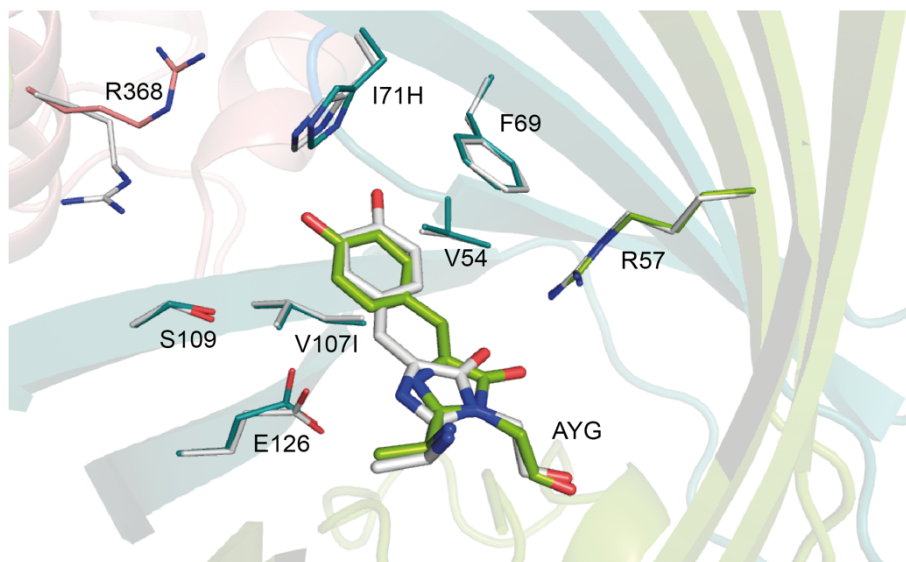
Supplementary Table 2. Data collection and refinement statistics for the structures elucidated in this work (Table 1).

Data collection	rsGCaMP1.1 eq	rsGCaMP1.1 illuminated (OFF)	rsGCaMP1.2 eq	rsGCaMP1.2 illuminated (OFF)	rsGCaMP1.3 eq
PDB ID	6YA9	6TV7	6ZSM	6ZSN	7AUG
Beamline	SLS PXIII X06DA	SLS PXIII X06DA	SLS PXIII X06DA	SLS PXIII X06DA	SLS PXIII X06DA
Wavelength	1.00	0.999995	1.00	1.00	0.999995
Space group	$P4_12_12$	$P4_12_12$	$P4_12_12$	$P4_12_12$	$P4_12_12$
Cell dimensions a, b, c (Å)	119.43, 119.43, 96.62	120.67, 120.67, 96.02	121.54, 121.54, 96.96	118.97, 118.97, 96.23	121.85, 121.85, 96.12
No. of molecules per asymmetric unit	1	1	1	1	1
Resolution (Å)	50–2.15 (2.20–2.15)	50–2.9 (2.98–2.90)	50–1.95 (2.00–1.95)	50–2.6 (2.67–2.60)	50–2.04 (2.16–2.04)
$I / \sigma I$	18.7 (2.1)	11.17 (1.6)	22.8 (1.9)	11.8 (1.6)	9.7 (1.3)
CC (1/2)	99.9 (74.6)	99.6 (64.1)	100 (67.4)	99.8 (61.6)	99.7 (48.4)
Completeness (%)	99.8 (100)	100 (99.9)	100 (100)	100 (100)	99.9 (99.6)
Redundancy	19.2 (20.3)	13.0 (13.2)	13.3 (13.8)	13.0 (12.5)	10.6 (10.4)
Refinement					
Resolution (Å)	2.15	2.50	1.95	2.60	2.04
No. reflections	38,513	15,423	53,375	21,798	46,902
$R_{\text{work}} / R_{\text{free}}$	18.7/23.1	18.2/25.0	15.7/19.8	19.1/25.9	16.5/20.7
No. atoms					
Protein	3,201	3,176	3,218	3,169	3,248
Water	233	88	444	108	346
Other	7	9	67	23	95
B -factor overall	52.2	55.9	41	63	44
R.m.s. deviations					
Bond lengths (Å)	0.010	0.010	0.018	0.007	0.012
Bond angles (°)	1.74	1.90	2.17	1.64	1.78
Ramachandran plot					
Most favored (%)	98	92	98	95	98
Additional allowed (%)	2	7	2	5	2

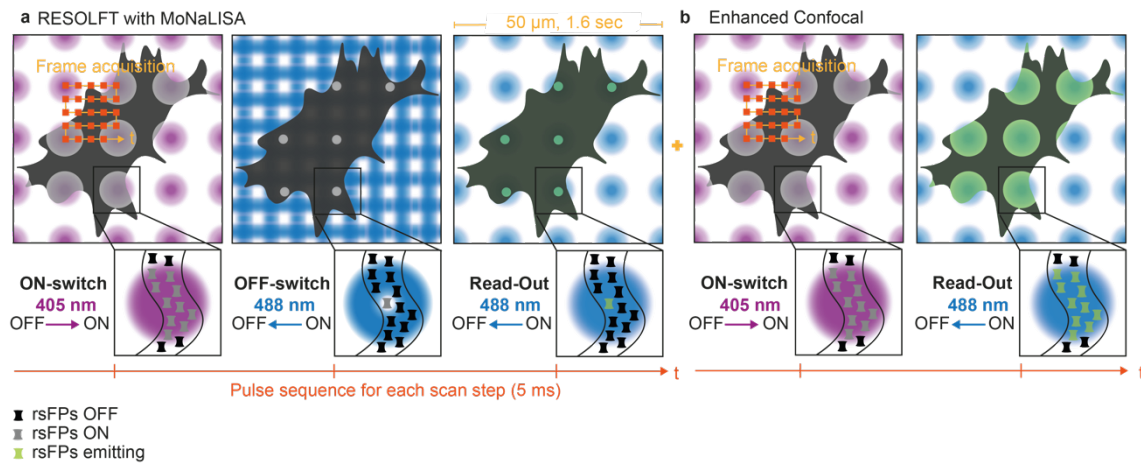
*Values in parentheses are for highest-resolution shell

Supplemental Information 3: Crystal Packing.

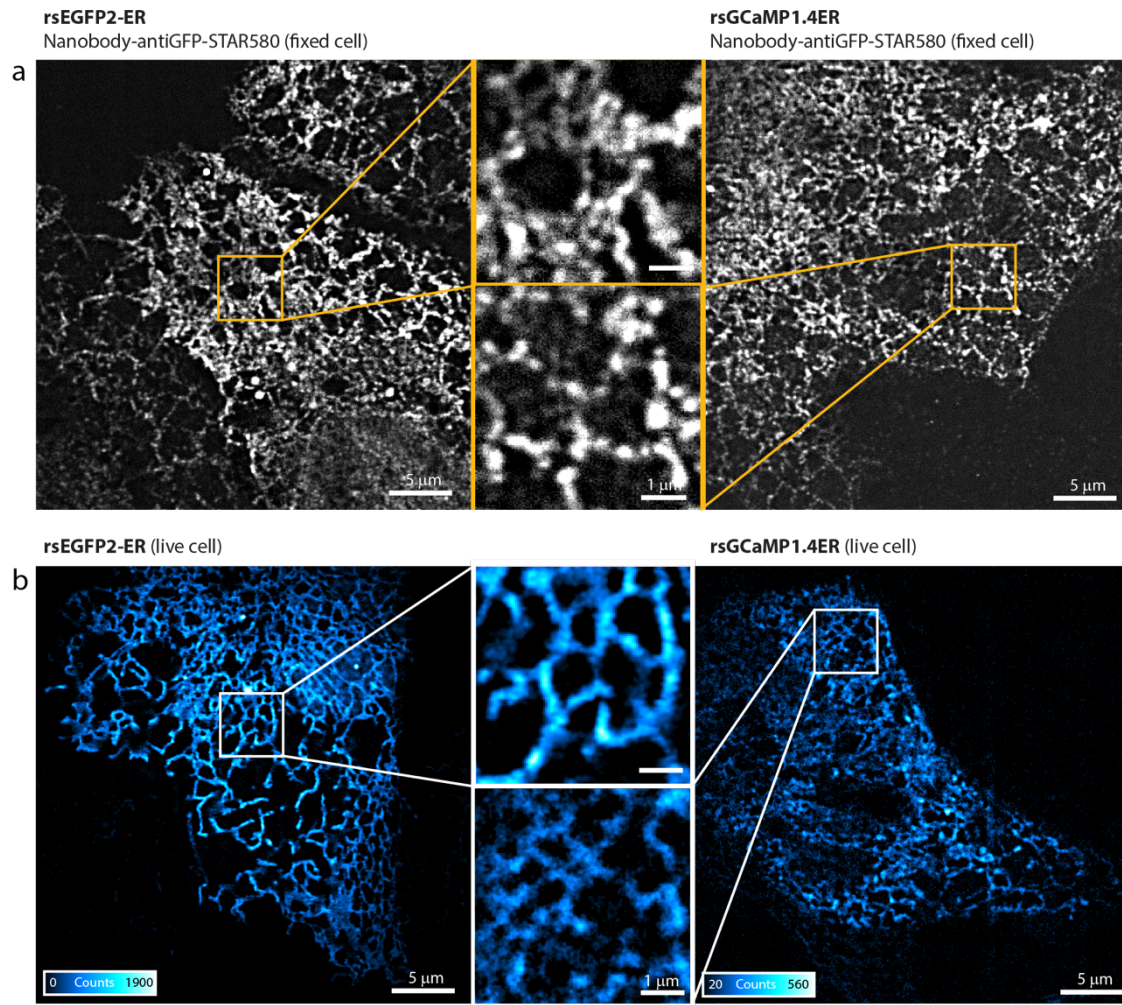
We assessed the possibility that the crystal-packing compresses the β -barrel of rsGCaMP1.1 and thus results in the observed hula-twist. We considered a similar scenario to that observed by Chang in 2019¹¹ for the artificially dehydrated and thus compressed unit cell of rsEGFP2. First, we assessed the water content of the unit cell of rsGCaMP1.1 in comparison to rsEGFP2 and dehydrated rsEGFP2. While the latter two show a low hydration of 38% and 31% respectively, the unit cell of rsGCaMP1.1 has a hydration of 66%, suggesting relatively loose crystal packing. Next, we analyzed the temperature factors (B-factors), which provide information about the mobility of the respective regions. The Calmodulin+M13 moiety in rsGCaMP1.1 is more mobile (-66.0) compared to the beta-barrel (-47.5). Therefore, a pronounced restriction of Calmodulin+M13, which could extend to the barrel side made up by beta-strand 7, 8, 10, is not suspected. This is also reflected in the observed low number of crystal contacts of Calmodulin+M13. Finally, we compared whether the crystal-contacts present in the dehydrated and compressed unit cells in Chang could act similarly on parts of the beta-barrel in rsGCaMP1.1; however, this was not the case. From this we conclude that neither the Calmodulin packed against beta-strands 7,8,10, nor the barrel itself, is in anyway restricted in a way that would explain the hula-twist based on crystal packing. Thus, we conclude that the unusual hula-twist in rsGCaMP1.1 indeed stems from the packing of the biological-interface between Calmodulin+M13 and the β -barrel, which could be expected in a similar fashion in solution.



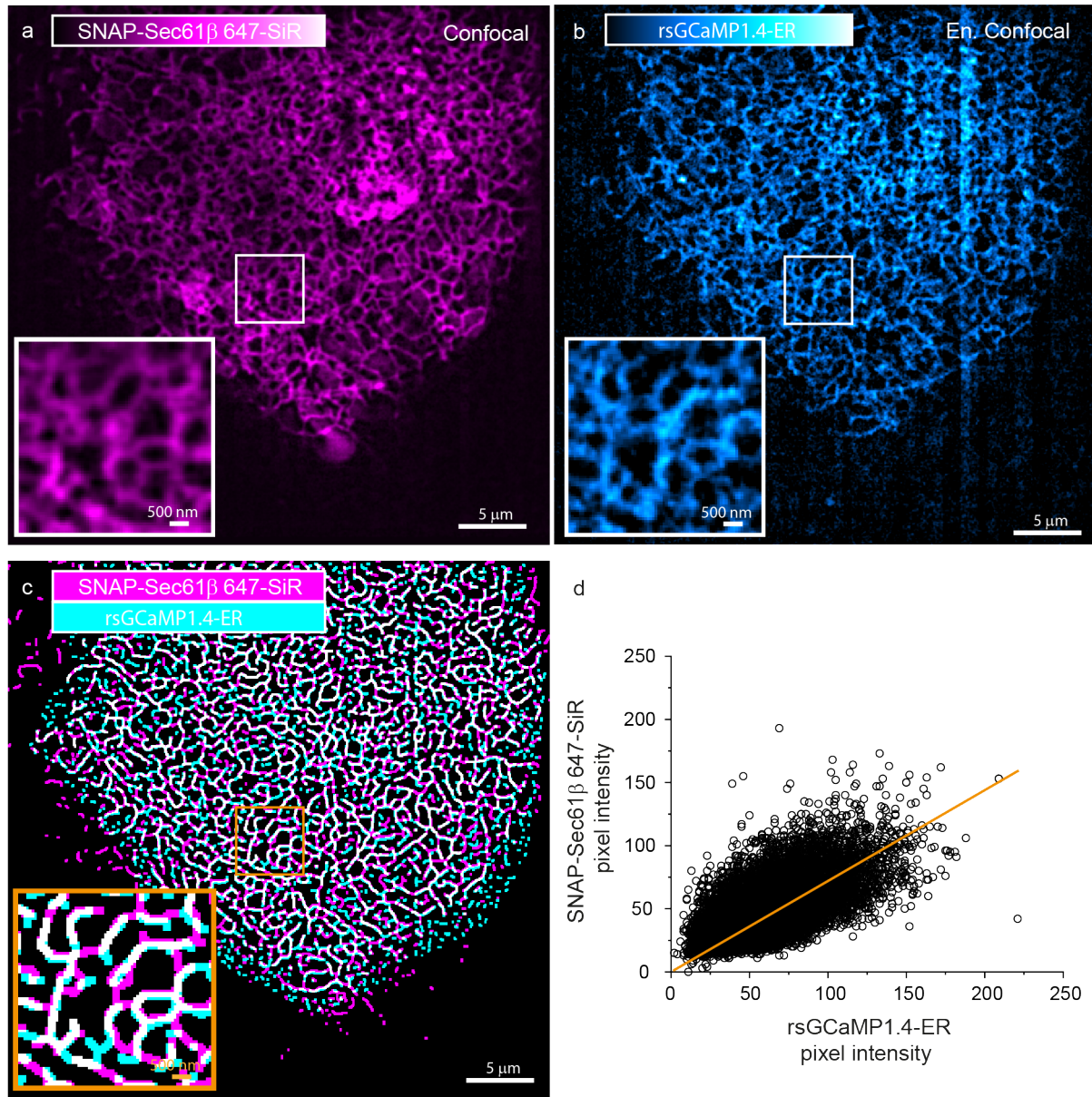
Supplemental Figure 10: Equilibrium and photo-switched structure of rsGCaMP1.2. Equilibrium structure color coded in teal, green and salmon (CaM) like in Figure 2b. Photoswitched structure in gray. The cartoon is only shown for the equilibrium state structure.



Supplementary Figure 11: Data acquisition of MoNaLISA and enhanced confocal: **a** Diagram of the acquisition procedure for the MoNaLISA implementation of the RESOLFT concept. In each scanning position the rsFPs are first driven to the on-state via illumination with 405 nm light, this diffraction-limited volume is subsequently shrunk switching off the molecule in the periphery using a 488 nm illumination, with the beam featuring a zero intensity in the center of the previously illuminated spot. Finally, this sub-diffracted volume is readout through a third 488 nm illumination. In a parallelized architecture this principle is implemented using different light patterns, multi-spots for on-switch and readout and grid-like interference pattern for the off-switching. To read the whole image it is then sufficient to scan only the period in between the multi-foci pattern, repeating the same illumination sequence for each scanning step. **b** Diagram of the acquisition procedure for the Enhanced Confocal starting in an imaging sequence with a delay of ~ 15 s. If the off-switching is not performed the whole diffraction limited volume imprinted in the on-switching is excited and registered, resulting in the enhance confocal image. The acquisition of the two image is sequential. Enhanced confocal is an imaging concept described in Masullo et al. Nat. Comm. 2018¹² and Dreier et al. Nat. Comm. 2019¹³. The main point is that the spatial resolution of the images produced by “enhanced” confocal is better (by a factor 1.4) than “conventional” confocal applied to non-switchable markers, such as GFP or Alexa488. The reason for this enhancement is that reversibly photoswitchable proteins used for enhanced confocal allow a two-step spatial confinement: one during the on-switching (for rsFPs like the one used in this study, 405 nm) and the second during readout (488 nm). The effective emitting volume results from this two-step absorption, and is therefore smaller than a single process.



Supplemental Figure 12: Controls for rsGCaMP1.4-ER Ca^{2+} imaging validity. The expression distribution in the ER of rsGCaMP1.4-ER was tested in comparison with the well-established non-sensor rsFP, rsEGFP2, and both together in fixed (a) and live (b) conditions. **a** In fixed cells the subcellular distribution of the two proteins was tested via immunostaining using nanobody-antiGFP-STAR580. The images are representative of 5 repetitions (n=5). **b** For the comparison in living cells, one frame recorded at the same on-switching, read-out powers, and times is reported. The images come from 4 independent days of measurements.



Supplementary Figure 13. Visualization of the ER network through lumen Ca^{2+} imaging (rsGCaMP1.4ER) and membrane localization (Sec61 β -SNAP 647-SiR) of fluorescent markers. Confocal images of (a) Sec61 β -SNAP 647-SiR (magenta) and (b) rsGCaMP1.4-ER (blue), acquired quasi-simultaneously in a pixel-by-pixel fashion for a pixel size of 75 nm and a scanning period of 625 nm (total frame time of 1.5 sec). The dwell time in each pixel is divided in 5 ms of 594 nm excitation for the 647-SiR channel, followed by 250 μs of 405 nm and 1 ms of 488 nm light to register the rsGCaMP1.4-ER signal. c Overlay of the skeleton for the two channels. The skeleton is obtained after an intensity threshold over the image filtered with a Laplacian filter of 2 pixels and dilated of 1 pixel for a clearer visualization. d Scatter plot between the pixel of the two images to visualize their colocalization. The images are representative of 5 repetitions (n=5).

Supplemental Information 4: rsGCaMP and MoNaLISA imaging considerations

The brightness difference between rsEGFP2 and rsGCaMP1.4ER, is also reflected in the imaging by a ~3-4 fold dimmer signal from rsGCaMP1.4ER. In order to better analyze the influence of the decreased signal-to-noise ratio in judging the morphological feature of the ER network, we artificially lowered the signal of rsEGFP2-ER to the expected range of rsGCaMP1.4-ER. The two proteins have identical cellular localization and similar resolution ability, giving us the possibility to fairly compare them for the different imaging modalities used.

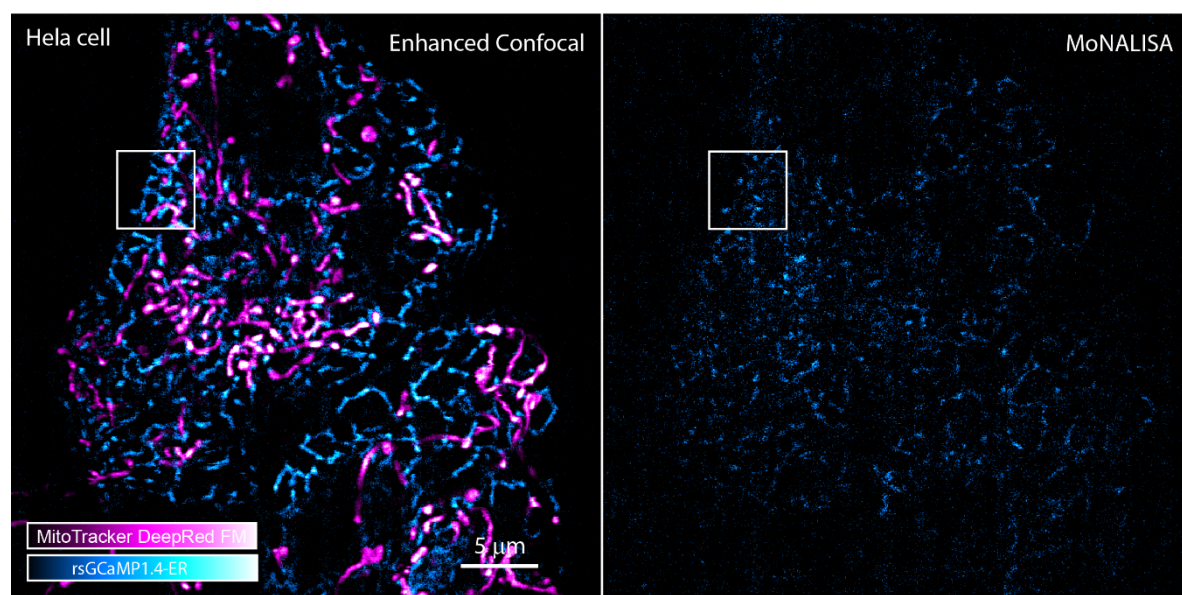
To scale properly the noise level of an acquired image, we assume that it can be expressed as a Poisson variable describing the fluorophore emission and a Gaussian distribution describing the read-out noise: $I_{x,y} = P(\alpha * \mu_{x,y}) + N(0, \sigma^2)$, where α is the brightness of the structure and σ the standard deviation of the read-out noise. Under this assumption, the variance of a pixel in the image is $Var(I_{x,y}) = \alpha\mu_{x,y} + \sigma^2$. If the image is simply rescaled, the associated variance would be $Var(kI_{x,y}) = k^2(\alpha\mu_{x,y} + \sigma^2)$, underestimating the fluctuation of the noise in case of a down-scaling ($k < 1$). To account for this discrepancy, the extra variance is therefore added to the rescaled image.

We focused on MoNaLISA images of rsEGFP2-ER and rsGCaMP1.4-ER when making comparisons at equal SNR because the smaller sub-diffracted volume probed imposes higher demands on the minimum level of signal required to record an image. When down-scaled by a factor of 4, the dimmer structures of rsEGFP2-ER fade into the background, resulting in a more fragmented distribution of the signal for the lumen localization similar to that recorded for a single frame of rsGCaMP1.4-ER.

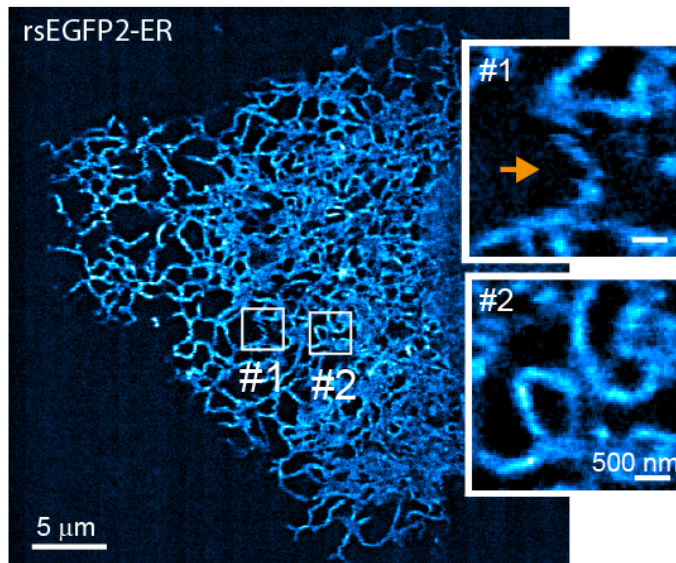
Experimentally for rsGCaMP1.4-ER, we can take advantage of the high photo-stability of rsGCaMP1.4-ER to increase the contrast of imaging by frame averaging (1-10 frames). This enables the use of rsGCaMP1.4-ER to describe the ER network with higher resolution ability. The frame averaging is, however, linked to the time accessibility of the probe, which in the specific cases recorded in this study vary between 1.6 sec (single frame) and 16 sec (10 averaged consecutive frames).

Given the sensor's dependency on Ca^{2+} and the increased resolution with which we are investigating the system, the fluorescence distribution will always be the convolution between the concentration of the protein construct and the nanoscale local Ca^{2+} concentration. For the specific case of rsGCaMP1.4-ER, this can further influence the sparsity of the signal.

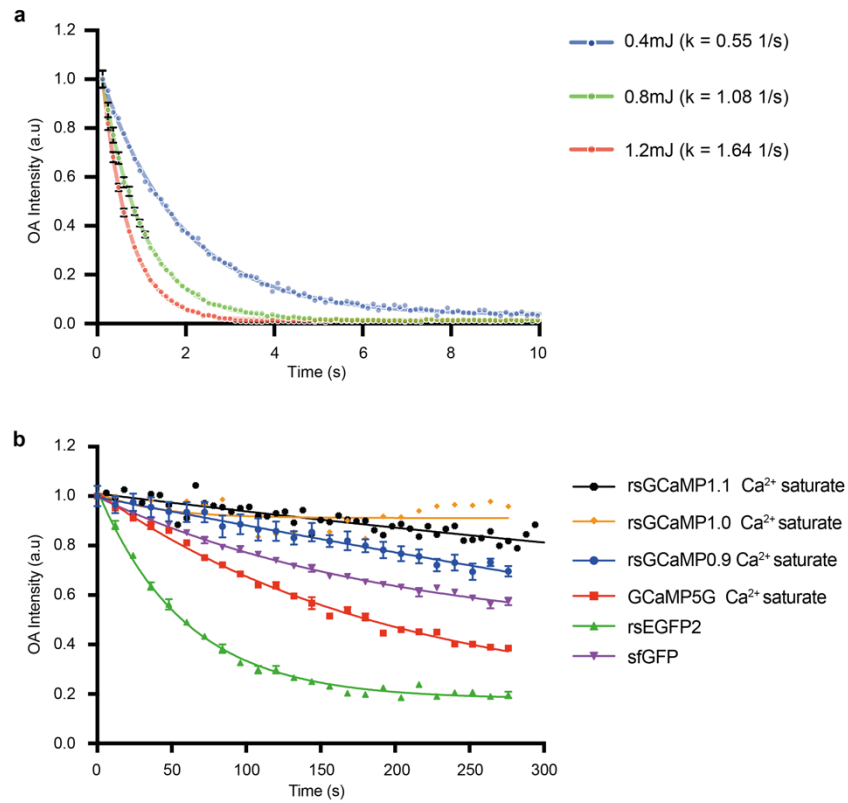
The fast kinetic of the probe indeed allow to push the speed of the technique, focusing on the nanoscale dynamics of Ca^{2+} domain in the context of the ER network. The combination with a parallelized recording gives the possibility to decouple speed of acquisition from the field of view recorded. This open the possibility to follow the nanoscale dynamics of Ca^{2+} over extended field of view without losing speed, being able to correlate events over the full cell extension and in cell-to-cell interaction.



Supplemental Figure 14. Live cell MoNaLISA imaging of rsGCaMP-ER in HeLa cells with live mitochondria staining (MitoTracker DeepRed FM). The image is the complete field-of-view of the inset presented in Figure 3c (rectangle). The images are representative of 3 repetitions (n=3).



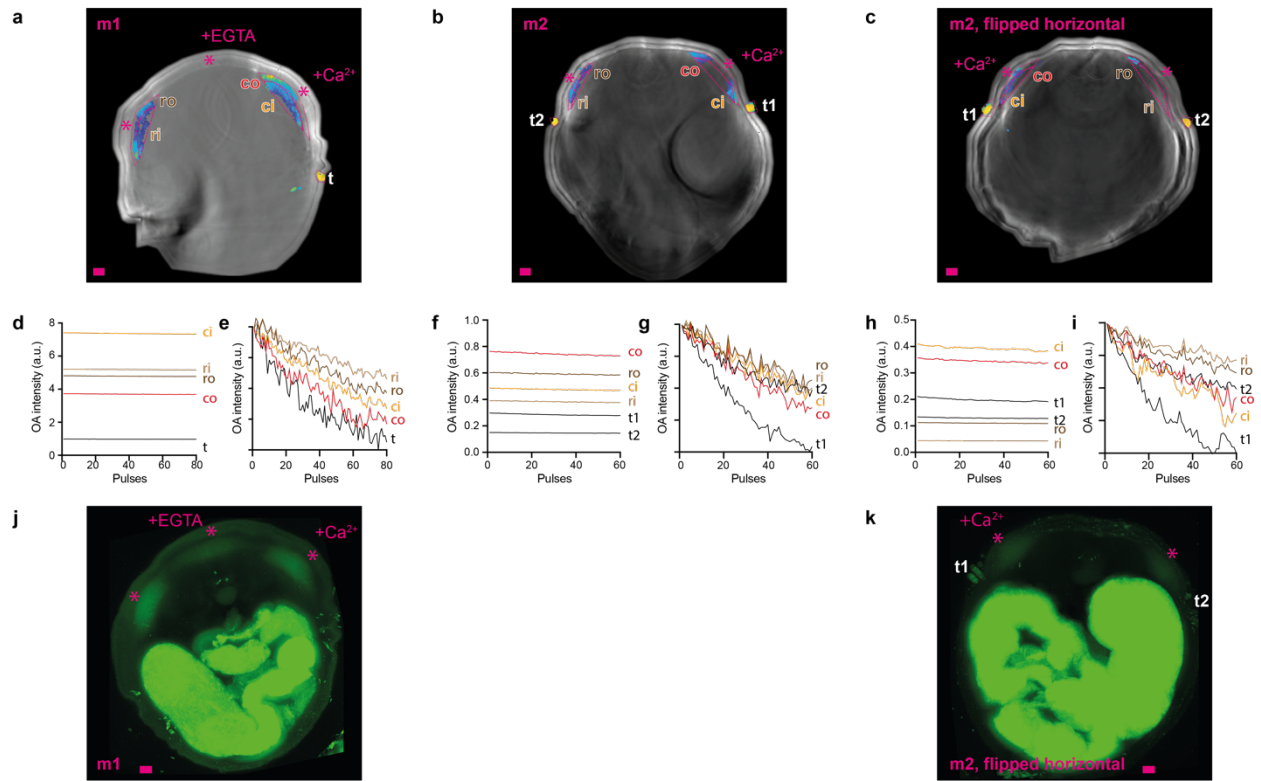
Supplementary Figure 15. Examples of movement artefacts. Representative MoNaLISA image of rsEGFP2-ER acquire at a frame rate of 1.7 s, where two details on the ER network are highlighted and enlarged. The images are representative of 10 repetitions (n=10).



Supplemental Figure 16: Characteristics of rsGCaMPs in OA illumination. **a** OFF-switching traces of rsGCaMP1.1 at Ca^{2+} saturation ($39 \mu\text{M}$) with different laser energies. The mean and standard deviation of three representative photo-switching cycles of a single measurement per condition are shown ($n=1$). All data was recorded using an analytical OA spectrophotometer¹⁴. Details can be found in the method section. Energies as stated for Figure 3e-g **b** Photofatigue of selected rsGCaMPs, GCaMP5G, rsEGFP2 and sfGFP under OA imaging conditions. All data was recorded using an analytical OA spectrophotometer described in the methods section. For the switchable proteins (rsGCaMPs and rsEGFP2) the maximum of each switching cycle is shown; for non-switching proteins the same illumination schedule was applied. Shown are the mean of three pulses with standard deviation. Protein concentration for all proteins measured was $30 \mu\text{M}$. Ca^{2+} saturated condition refers to $39 \mu\text{M}$.

Supplementary Information 5: OA imaging with different geometries:

We demonstrate *in vitro* that the signal from rsGCaMP can be readily unmixed from blood – a major confounder in *in vivo* imaging – making the blood background virtually invisible. We used tubing filled with purified rsGCaMP mixed with different concentrations of Ca^{2+} , as well as tubings filled with blood. We recorded data by illuminating the tubings with 488 nm and 420 nm light using a 64-element array (Extended Data 8a-c) and a scanning style imaging system (Extended Data 8d-f). While in the raw data, rsGCaMP is barely detectible over the strong signal of blood (top images of Extended Data 8a and 8d), the blood signal is completely gone in the unmixed data and rsGCaMP is visible at all concentrations (bottom images). Analyzing the mean kinetics of the unmixed tubings (Extended Data 8b) or the differentials between 488 nm and 488/405 nm (Extended Data 8e) reveals different kinetic constants fitting a sigmoidal with a similar K_D range, as found for absorbance and OA-spectroscopy (Extended Data 8c and f). Differences in the K_D are likely the result of the very difference measurement and analysis conditions of the methods.



Supplemental Figure 17. Additional MSOT imaging of rsGCaMP1.1. *In vivo* imaging of *sub cutaneous* implants of HeLa cells expressing rsGCaMP1.1 (2.5 million cells) as in in Figure 31-n. For mouse 1 (a, d, e and j), for one implant, the cells were pretreated with 5 μ M Ionomycin and 10 mM of Ca²⁺ (“+Ca²⁺”), for another implant with 5 μ M Ionomycin and 5 mM EGTA (“+EGTA”), and for yet another implant the cells were untreated. For mouse 2 (b-c, f-i and k), for one implant, the cells were pretreated with 5 μ M Ionomycin and 10 mM of Ca²⁺ (“+Ca²⁺”) and for one implant left without treatment. Mouse 2 has been imaged in 2 orientations (b, f-g as well as c, h-i and k). Abbreviation as well as label and plot color indicate the type of the implant / region-of-interest: “ri” = resting inner, “ro” = resting outer, “ci” = Ca²⁺ inner, “co” = Ca²⁺ outer, t, t1 and t2, respectively, denote control tubes attached to the skin of the mouse. In total this amounts to 3 independent measurements (n=3).

The cells signal can be cleanly separated from background exploiting the photo-switching characteristics of rsGCaMP1.1. Additionally, the relative Ca²⁺ concentration can be tentatively inferred from the mean switching kinetics of the implants (d-i). d,f and h show the raw data mean kinetic of the ROIs in (a-c) while e, g and i show the kinetics normalized to their maxima. It should be noted that the kinetic discrimination is poor due to the strong impact of light fluence changes due to the used visible wavelengths strongly absorbing in tissue. Scalebar is 1 mm. Description of the analysis can be found in Supplemental Figure 18, energies as in Figure 31. Note that the autofluorescence of the intestine saturates the GFP-channel in this area.

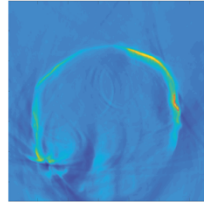
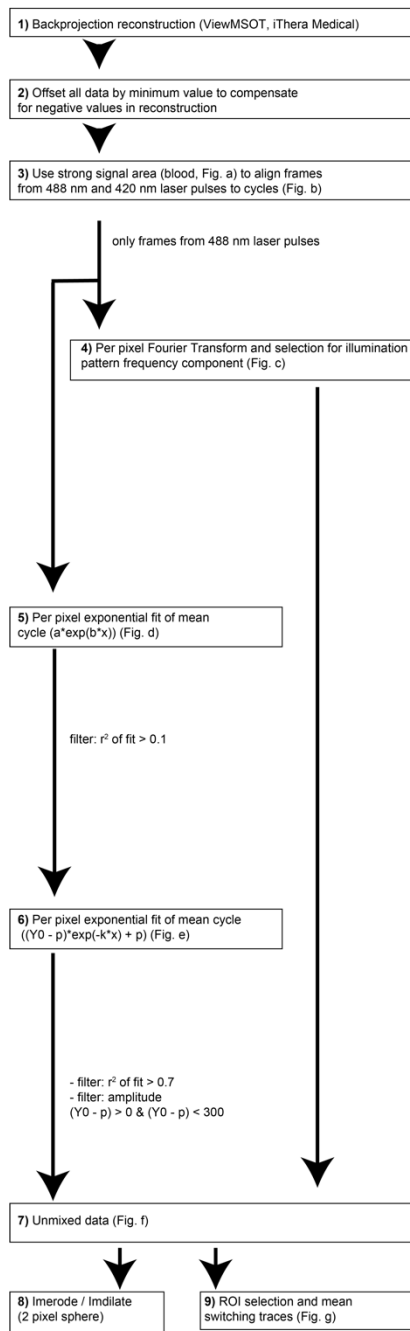


Fig. a.: Strong signal ROI (pink)

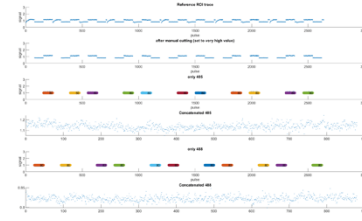


Fig. b.: Mean trace for ROI showing the assignment process

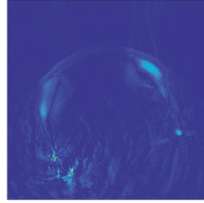


Fig. c.: Intensity of frequency peak (and 1st 3 harmonics) fitting to illumination pattern frequency

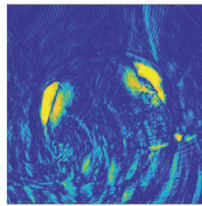


Fig. d.: $(a \cdot \exp(b \cdot x))$ per pixel

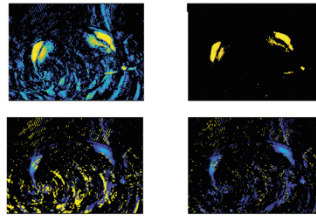


Fig. e.: r^2 result for 5) and 6) and filtered (left) and amplitude result and filtered (right)

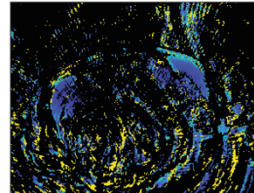


Fig. f.: k from 6 filtered by fit, r^2 and amplitude (from 6)

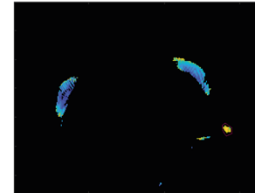
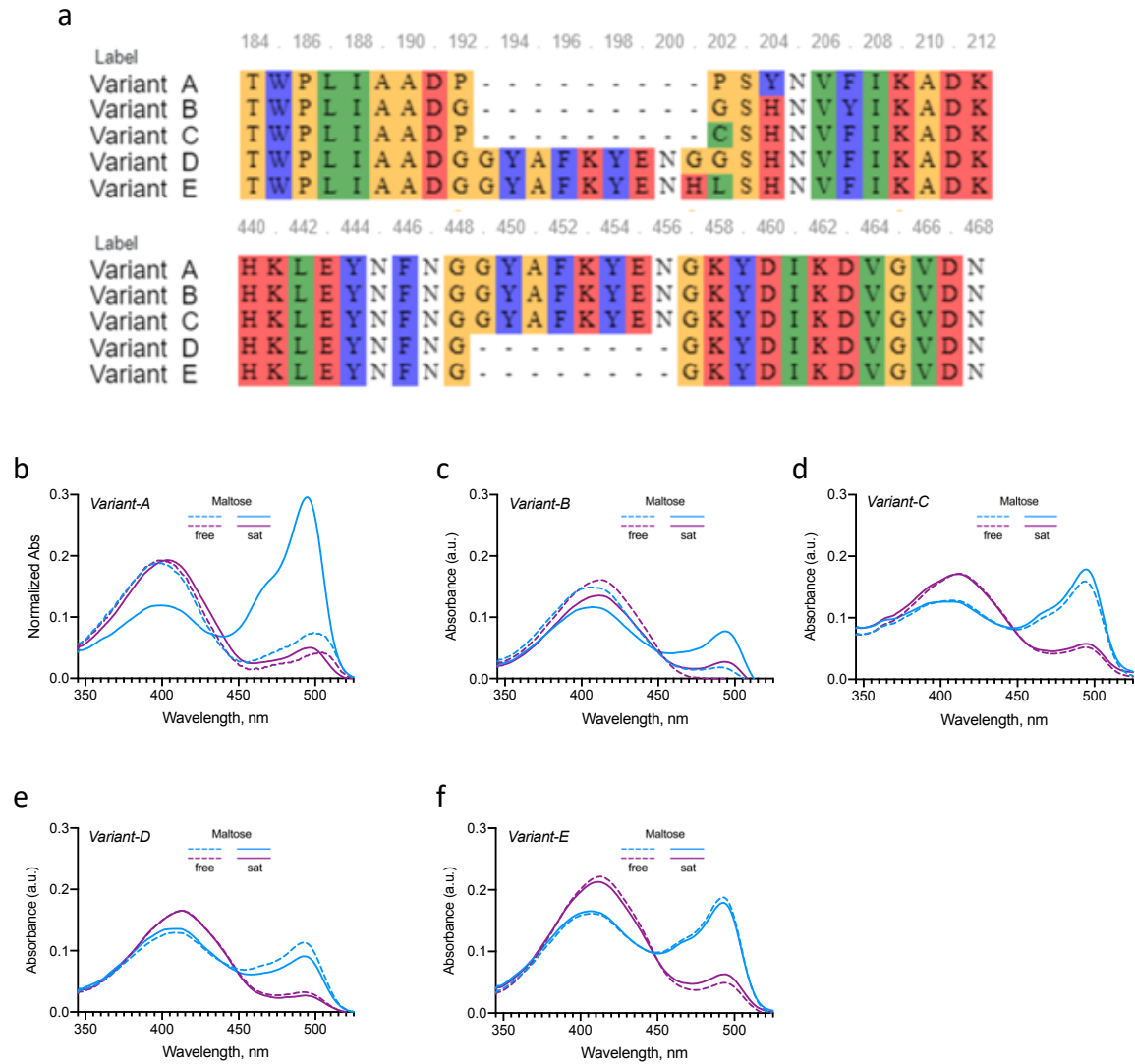


Fig. g.: Exemplary switching trace from exemplary ROI (f)

Supplemental Figure 18. Description of the analysis procedure for *in vivo* MSOT measurements of rsGCaMP1.1. The procedure is detailed using mouse 1 as an example.



Supplemental Figure 19: Sequence alignment and spectral characterization of reversible switchable maltose sensor. We introduced the mutations that confer photo-switching in rsGCaMP0.9 in the different variants of the maltose sensor described in Marvin et al.¹⁵ (linker and MBP insertion position). The resulting variants showed markedly different effects of the photo-switching mutations. **a** The sequence alignment for the linker regions of the different constructs. Along the lines of the original variants of the maltose sensor, in **Variant A-C** switchable cpGFP sequence from rsGCaMP0.9 is inserted at position 165 of MBP domain with linker PPYF, PCF, and GGS respectively. In **Variant D-E** switchable cpGFP sequence from rsGCaMP0.9 is inserted at position 173 of MBP domain with linker GGS and HLS respectively. Leading to **VariantA** = rsMBP165-PPYF, **VariantB** = rsMBP165-PCF, **VariantC** = rsMBP165-GGS, **VariantD** = rsMBP173-GGS and **VariantE** = rsMBP173-HLS, respectively; the numbering follows the original maltose sensor¹⁵. **b-f** The ON state (after 405 nm illumination, cyan) and OFF state (after 488nm illumination, purple) spectra of five different constructs in the Maltose-saturated (solid) and Maltose-free states (dotted). Only **VariantA** showed maltose sensitivity with significant photo-switching. Data shown for representative single measurements (n=1), only **VariantA** recorded as triplicates (n=3) with mean and errors reported in Supplementary Table 3. Illumination conditions are given in Extended Data Table 1.

Supplemental Table 3: Photophysical characteristics of developed photoswitching Maltose sensor variants.
Data recorded as triplicates (n=3) shown is the mean with standard deviation.

	Absorbivity ($M^{-1} cm^{-1} \times 1000$)	Quantum Yield (%)	Molecular Brightness ^a	Affinity	Malt. Response (%) ^b	Swiching (%) ^c
rs/cpGFP-MBP	31.4 ± 0.8	32.4 ± 5	10.2	12.0 ± 1.1 μM	78.8 ± 2.4	72.6 ± 5.6
cpGFP-MBP^d	12.2	68	8.3	5 μM^d	64	/

a) Molecular brightness as: (QY * Absorptivity) / 10,000

b) Malt. Response (%) was calculated as the differential between On state fluorescence in presence of maltose minus On state in absence of maltose divided by the On state in presence of maltose.

c) Fluorescence switching (%) was calculated as the differential between On state (after 405 illumination) and off state (after 490 illumination) divided by the On State.

d) Marvin, *Proteins*, 2011: variant MBP165-cpGFP.PPYF

Supplemental Information Bibliography

1. de Juan-Sanz, J., Holt, G. T., Schreiter, E. R., de Juan, F., Kim, D. S. & Ryan, T. A. Axonal Endoplasmic Reticulum Ca²⁺ Content Controls Release Probability in CNS Nerve Terminals. *Neuron* **93**, 867–881.e6 (2017).
2. Henderson, M. J., Baldwin, H. A., Werley, C. A., Boccardo, S., Whitaker, L. R., Yan, X., Holt, G. T., Schreiter, E. R., Looger, L. L., Cohen, A. E., Kim, D. S. & Harvey, B. K. A low affinity GCaMP3 variant (GCaMPer) for imaging the endoplasmic reticulum calcium store. *PLoS One* **10**, (2015).
3. Gee, J. M., Smith, N. A., Fernandez, F. R., Economo, M. N., Brunert, D., Rothermel, M., Morris, S. C., Talbot, A., Palumbos, S., Ichida, J. M., Shepherd, J. D., West, P. J., Wachowiak, M., Capecchi, M. R., Wilcox, K. S., White, J. A. & Tvrdik, P. Imaging Activity in Neurons and Glia with a Polr2a-Based and Cre-Dependent GCaMP5G-IRES-tdTomato Reporter Mouse. *Neuron* **83**, 1058–1072 (2014).
4. Akerboom, J. *et al.* Optimization of a GCaMP calcium indicator for neural activity imaging. *J. Neurosci.* **32**, 13819–13840 (2012).
5. Grotjohann, T., Testa, I., Reuss, M., Brakemann, T., Eggeling, C., Hell, S. W. & Jakobs, S. rsEGFP2 enables fast RESOLFT nanoscopy of living cells. *Elife* **2012**, 1–14 (2012).
6. Helassa, N., Zhang, X. H., Conte, I., Scaringi, J., Esposito, E., Bradley, J., Carter, T., Ogden, D., Morad, M. & Török, K. Fast-Response Calmodulin-Based Fluorescent Indicators Reveal Rapid Intracellular Calcium Dynamics. *Sci. Rep.* **5**, 1–15 (2015).
7. Helassa, N., Podor, B., Fine, A. & Török, K. Design and mechanistic insight into ultrafast calcium indicators for monitoring intracellular calcium dynamics. *Sci. Rep.* **6**, 1–14 (2016).
8. Wu, J., Prole, D. L., Shen, Y., Lin, Z., Gnanasekaran, A., Liu, Y., Chen, L., Zhou, H., Chen, S. R. W., Usachev, Y. M., Taylor, C. W. & Campbell, R. E. Red fluorescent genetically encoded Ca²⁺ indicators for use in mitochondria and endoplasmic reticulum. *Biochem. J.* **464**, 13–22 (2014).
9. Akerboom, J., Rivera, J. D. V., Guilbe, M. M. R., Malavé, E. C. A., Hernandez, H. H., Tian, L., Hires, S. A., Marvin, J. S., Looger, L. L. & Schreiter, E. R. Crystal structures of the GCaMP calcium sensor reveal the mechanism of fluorescence signal change and aid rational design. *J. Biol. Chem.* **284**, 6455–6464 (2009).
10. Chen, Y., Song, X., Ye, S., Miao, L., Zhu, Y., Zhang, R.-G. & Ji, G. Structural insight into enhanced calcium indicator GCaMP3 and GCaMPJ to promote further improvement. *Protein Cell* **4**, 299–309 (2013).
11. Chang, J., Romei, M. G. & Boxer, S. G. Structural Evidence of Photoisomerization Pathways in Fluorescent Proteins. *J. Am. Chem. Soc.* **141**, 15504–15508 (2019).
12. Masullo, L. A., Bodén, A., Pennacchietti, F., Coceano, G., Ratz, M. & Testa, I. Enhanced photon collection enables four dimensional fluorescence nanoscopy of living systems. *Nat. Commun.* **9**, (2018).
13. Dreier, J., Castello, M., Coceano, G., Cáceres, R., Plastino, J., Vicidomini, G. & Testa, I. Smart scanning for low-illumination and fast RESOLFT nanoscopy in vivo. *Nat. Commun.* **10**, 556 (2019).
14. Fuenzalida Werner, J. P., Huang, Y., Mishra, K., Chmyrov, A., Ntziachristos, V. & Stiel, A. C. Challenging a preconception: Optoacoustic spectrum differs from the absorption spectrum of proteins and dyes for molecular imaging. *BioRxiv* (2020) doi:10.1101/2020.02.01.930230.
15. Marvin, J. S., Schreiter, E. R., Echevarría, I. M. & Looger, L. L. A genetically encoded,

- high-signal-to-noise maltose sensor. *Proteins* **79**, 3025–3036 (2011).
16. Patriarchi, T., Cho, J. R., Merten, K., Howe, M. W., Marley, A., Xiong, W.-H., Folk, R. W., Broussard, G. J., Liang, R., Jang, M. J., Zhong, H., Dombeck, D., von Zastrow, M., Nimmerjahn, A., Gradinaru, V., Williams, J. T. & Tian, L. Ultrafast neuronal imaging of dopamine dynamics with designed genetically encoded sensors. *Science* (80-.). **360**, eaat4422 (2018).